APL Materials

Synthesis science of $SrRuO_3$ and $CaRuO_3$ epitaxial films with high residual resistivity ratios

Cite as: APL Mater. **6**, 046101 (2018); https://doi.org/10.1063/1.5023477
Submitted: 24 January 2018 • Accepted: 05 March 2018 • Published Online: 04 April 2018

Hari P. Nair, Yang Liu, Jacob P. Ruf, et al.

ARTICLES YOU MAY BE INTERESTED IN

Demystifying the growth of superconducting Sr_2RuO_4 thin films
APL Materials **6**, 101108 (2018); https://doi.org/10.1063/1.5053084

Magnetic Properties of $SrRuO_3$ and $CaRuO_3$
Journal of Applied Physics **39**, 1327 (1968); https://doi.org/10.1063/1.1656282

Epitaxial integration and properties of $SrRuO_3$ on silicon
APL Materials **6**, 086101 (2018); https://doi.org/10.1063/1.5041940

AIP Publishing

© 2018 Author(s).

APL MATERIALS 6, 046101 (2018)

Synthesis science of $SrRuO_3$ and $CaRuO_3$ epitaxial films with high residual resistivity ratios

Hari P. Nair,[1] Yang Liu,[2] Jacob P. Ruf,[2] Nathaniel J. Schreiber,[1] Shun-Li Shang,[3] David J. Baek,[4] Berit H. Goodge,[5] Lena F. Kourkoutis,[5,6] Zi-Kui Liu,[3] Kyle M. Shen,[2,6] and Darrell G. Schlom[1,6]
[1]*Department of Materials Science and Engineering, Cornell University, Ithaca, New York 14853, USA*
[2]*Department of Physics, Cornell University, Ithaca, New York 14853, USA*
[3]*Department of Materials Science and Engineering, The Pennsylvania State University, University Park 16802, Pennsylvania, USA*
[4]*School of Electrical and Computer Engineering, Cornell University, Ithaca, New York 14853, USA*
[5]*School of Applied and Engineering Physics, Cornell University, Ithaca, New York 14853, USA*
[6]*Kavli Institute at Cornell for Nanoscale Science, Ithaca, New York 14853, USA*

(Received 24 January 2018; accepted 5 March 2018; published online 4 April 2018)

Epitaxial $SrRuO_3$ and $CaRuO_3$ films were grown under an excess flux of elemental ruthenium in an adsorption-controlled regime by molecular-beam epitaxy (MBE), where the excess volatile RuO_x (x = 2 or 3) desorbs from the growth front leaving behind a single-phase film. By growing in this regime, we were able to achieve $SrRuO_3$ and $CaRuO_3$ films with residual resistivity ratios ($\rho_{300\,K}/\rho_{4\,K}$) of 76 and 75, respectively. A combined phase stability diagram based on the thermodynamics of MBE (TOMBE) growth, termed a TOMBE diagram, is employed to provide improved guidance for the growth of complex materials by MBE. © *2018 Author(s). All article content, except where otherwise noted, is licensed under a Creative Commons Attribution (CC BY) license (http://creativecommons.org/licenses/by/4.0/).*
https://doi.org/10.1063/1.5023477

The ruthenates host a myriad of exotic electronic and magnetic phenomena, including odd-parity superconductivity,[1] quantum criticality,[2] and electronic nematicity.[2–4] In many ruthenates, even very small amounts of disorder can mask the true ground state. For instance, the odd-parity superconductivity of Sr_2RuO_4 is the most disorder-sensitive superconductor known, where impurity concentrations in the range of only hundreds of ppm[5] or structural disorder[6] can destroy the superconducting ground state. In the case of $CaRuO_3$, only recently have films with very low residual resistivities helped to reveal a Fermi liquid ground state below 1.5 K, where previous studies suggested non-Fermi liquid behavior.[7] Moreover, the properties of ruthenates are known to respond dramatically to dimensionality,[8–10] strain,[11–13] and pressure,[14,15] making them an ideal system for exploring the effects of biaxial strain and dimensional confinement in epitaxial thin films. Therefore, the ability to synthesize ruthenate thin films with extremely low amounts of disorder will be crucial for understanding how their emergent properties and ground states can be manipulated and controlled in thin film form.

A significant issue during the growth of ruthenate thin films is the loss of ruthenium in the form of RuO_x ($x = 2, 3$, or 4).[16–18] The growth temperature at which this loss occurs depends on oxygen activity, but is typically above about 700 °C.[19–21] The films so produced contain ruthenium vacancies and have high residual resistivities.[19–27] In extreme cases, $SrRuO_3$ films exhibit semiconducting behavior in electrical transport measurements with $d\rho/dT < 0$ with a concomitant reduction in ferromagnetic T_c and an expansion in volume per formula unit.[19–28]

One approach to maintaining film stoichiometry is to grow at a low substrate temperature where the volatility of ruthenium (in the form of RuO_x) is negligible. Unfortunately significant structural disorder exists in such films, which limits their residual resistivity. The highest residual resistivity ratio (RRR), ($\rho_{300\,K}/\rho_{4\,K}$), reported for $SrRuO_3$ grown from a stoichiometric flux is 8.4.[29]

 © Author(s) 2018

Another approach is to grow at high substrate temperature where ruthenium volatility is significant and flood the growing film with excess ruthenium. This approach is analogous to the way in which high quality films of compound semiconductors with volatile constituents such as GaAs are grown.[30–38] The advantage of such an approach is that thermodynamics can be employed to automatically control film stoichiometry. The high growth temperature reduces disorder, and the automatic composition control provided by thermodynamics, within a range of growth conditions called a "growth window," can be harnessed to synthesize single-phase thin films with excellent electrical properties.

Adsorption-controlled growth of complex oxides[39–72] provides a pathway for achieving thin films with very low residual resistivities by mitigating defects resulting from cation non-stoichiometry. Indeed, $SrVO_3$ thin films with exceptionally low residual resistivities have been demonstrated using a metal-organic precursor for vanadium. Ruthenates, on the other hand, do not require a metal-organic precursor to access an adsorption-controlled growth window due to the high volatility of RuO_x species.[16–18] To date, the highest RRRs, ($\rho_{300\,K}/\rho_{4\,K}$), reported for thin films are ∼80 for an 80 nm thick $SrRuO_3$ film and 39 for a 78 nm thick $CaRuO_3$ film, respectively.[7,73] For comparison, the highest RRRs, ($\rho_{300\,K}/\rho_{4\,K}$), reported for single crystals of $SrRuO_3$ and $CaRuO_3$ are 162 and 38, respectively.[74,75] In general, the RRRs of perovskite ruthenate thin films have been low, likely due to the presence of ruthenium vacancies and more generally due to a lack of clear guiding principles for the growth of high-quality perovskite ruthenate thin films.

In this manuscript, we outline a thermodynamic growth window for the growth of $SrRuO_3$ and $CaRuO_3$ thin films in an adsorption-controlled regime utilizing high-purity elemental sources. Adsorption-controlled growth is critical for avoiding defects related to cation non-stoichiometry, which can be detrimental to electrical transport properties.

$SrRuO_3$ and $CaRuO_3$ epitaxial thin films were grown using a Veeco GEN10 molecular-beam epitaxy system. Strontium and calcium were evaporated from low-temperature effusion cells while an electron beam evaporator was used for ruthenium. All of the elemental source materials—strontium, calcium, and ruthenium—had a purity of 99.99%. Oxidation was achieved using either the output from a commercial ozone generator (∼10% O_3 + 90% O_2) or distilled ozone (∼80% O_3 + 20% O_2). The ozone + oxygen mixture was introduced through a water-cooled, electropolished 316L stainless steel tube with a 4.6 mm inner diameter pointed at the substrate with an angle of inclination of 40° from the normal of the substrate and that terminates at a distance of 9.6 cm from the center of the substrate. The tube provides an enhancement in the local oxidant pressure by a factor of ∼4× over the background chamber pressure. Substrate temperature was measured using a pyrometer. (110) $NdGaO_3$ substrates, from CrysTec GmbH, were etched using HF-NH_4OH and then annealed at 950 °C in flowing oxygen to yield a GaO_2-terminated surface.[76] (100) $SrTiO_3$ substrates were etched in buffered HF and annealed at 950 °C in flowing oxygen to yield a TiO_2-terminated surface.[77]

Figure 1(a) illustrates the pressure-temperature window under which different members of the $Sr_{n+1}Ru_nO_{3n+1}$ Ruddlesden-Popper (RP) series[78–80] are thermodynamically stable. The thermodynamic data for $Sr_{n+1}Ru_nO_{3n+1}$ are from electrochemical cell measurements,[81] while the thermodynamic data for ruthenium oxides are from Rard.[17] Note that Fig. 1(a) is a combination of two types of phase diagrams. The solid lines in the bottom half of Fig. 1(a) are the typical Ellingham diagram applied to the Sr-Ru-O ternary system with three solid phases in equilibrium with each other. Along those lines, the partial pressures of all species in the system are a function of temperature including the partial pressure of oxygen plotted in the diagram. In contrast, the dashed lines in the top half of the diagram denote the equilibria between two solid phases under a flux balance equation given as follows:

$$\Phi_{Ru} = \frac{1}{\sqrt{2\pi k T_s}}\left[\frac{p_{RuO_2}}{\sqrt{m_{RuO_2}}} + \frac{p_{RuO_3}}{\sqrt{m_{RuO_3}}}\right], \tag{1}$$

where Φ_{Ru} is the excess flux of ruthenium arriving at the substrate, k is the Boltzmann constant, T_s is the substrate temperature, p_{RuO_2} and p_{RuO_3} are the partial pressures of RuO_2(g) and RuO_3(g), respectively, and m_{RuO_2} and m_{RuO_3} are the molecular masses of RuO_2(g) and RuO_3(g), respectively. This flux balance is established by considering that the incoming excess flux of ruthenium to the substrate is balanced by the flux of ruthenium leaving the substrate in the form of RuO_x(g). In this diagram, the blue, purple, gold, and red lines represent the change of stability of $SrRuO_3$(s), $Sr_4Ru_3O_{10}$(s), $Sr_3Ru_2O_7$(s), and Sr_2RuO_4(s), respectively.

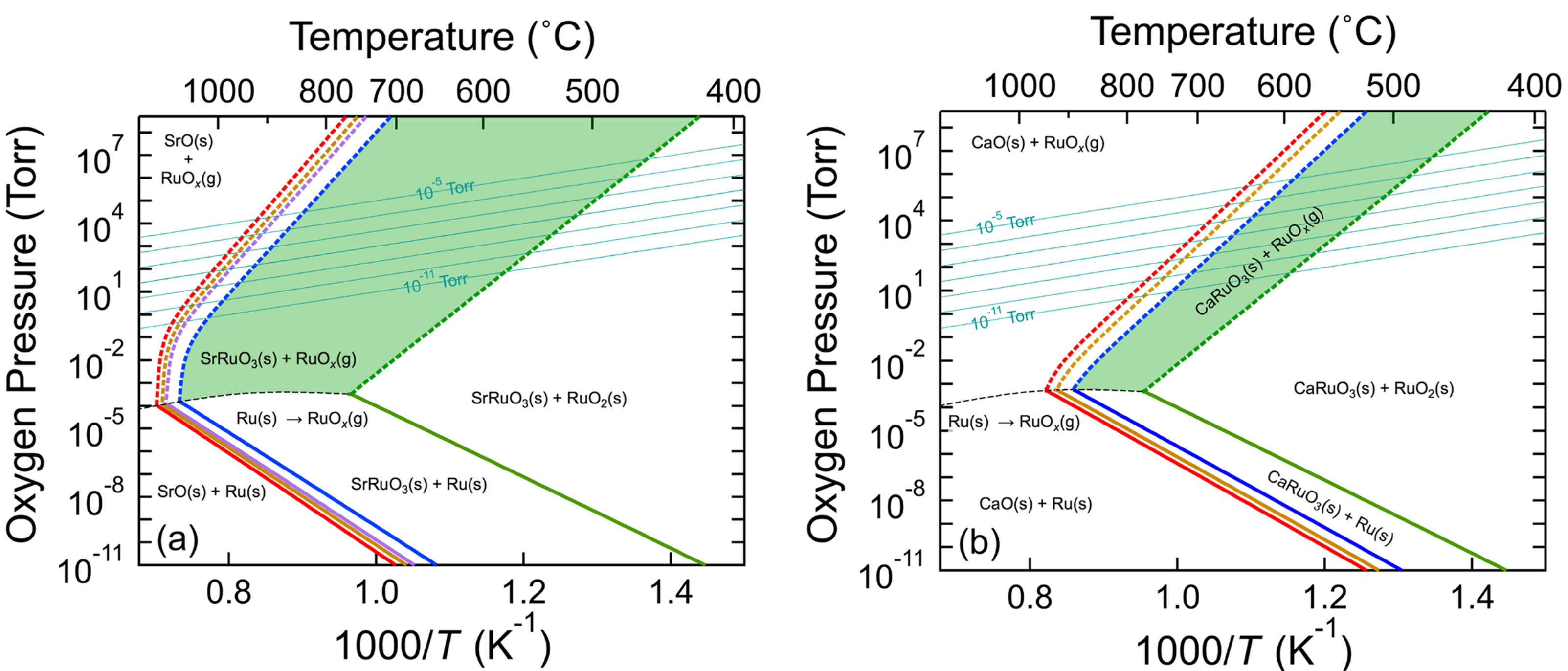

FIG. 1. TOMBE diagrams illustrating the adsorption-controlled growth window for (a) $Sr_{n+1}Ru_nO_{3n+1}$ and (b) $Ca_{n+1}Ru_nO_{3n+1}$ phases. The light green shaded regions in (a) and (b) are the adsorption-controlled growth windows for $SrRuO_3$ and $CaRuO_3$, respectively. The cyan lines show the equivalent oxidation potential for ozone partial pressures ranging from 10^{-11} to 10^{-5} Torr, illustrating the benefit of having ozone as an oxidant while maintaining the long mean free path necessary for MBE. An excess ruthenium flux of 1.95×10^{13} atoms/cm^2 s and 3.2×10^{13} atoms/cm^2 s was used in the thermodynamic calculations for (a) and (b), respectively.

This combined phase stability diagram is very useful in guiding the growth of complex phases by molecular-beam epitaxy (MBE). For oxygen partial pressures below the dotted black and dotted green lines, solid ruthenium or RuO_2 cannot be fully vaporized, and the conventional Ellingham diagram can be used to describe the phase relations as a function of temperature and oxygen partial pressure. At oxygen partial pressure above the dotted black and dotted green lines, however, solid ruthenium or RuO_2 is no longer stable with respect to the gas phase and is thus fully vaporized. Thermodynamic stability during MBE is consequently dictated by the equilibrium among species in the gas phase under a given overall ruthenium flux as dictated by Eq. (1). We call this combined phase stability diagram based on the thermodynamics of MBE (TOMBE) growth a TOMBE diagram.

In the TOMBE diagram [Fig. 1(a)], the light-green shaded region is the adsorption-controlled growth window for $SrRuO_3$, where solid $SrRuO_3$ is in equilibrium with RuO_x ($x = 2$ or 3) in the gas phase. Within this growth window, any excess ruthenium will desorb from the surface of the film as RuO_x(g) ($x = 2$ or 3), leading to the phase-pure epitaxial growth of $SrRuO_3$. Indeed, pausing growth within this window with the strontium shutter closed and the ruthenium shutter open results in a steady state situation where the $SrRuO_3$ film is stable and no phases are growing (neither $SrRuO_3$ nor any other phases). In the absence of an *A*-site cation (strontium or calcium), all of the incident ruthenium atoms are converted to RuO_x(g), which readily desorbs from the surface. This is analogous to the adsorption-controlled growth window for III-V compound semiconductors where the excess group V species desorb from the growth front.[30–38]

This adsorption-controlled growth window for $SrRuO_3$ [shaded in green in Fig. 1(a)] is bounded by various reactions. The dotted black line, representing the reaction of ruthenium metal with oxygen to form RuO_x(g), delineates the low oxygen pressure boundary below which excess ruthenium will precipitate as ruthenium metal. On the high-temperature side, it is bound by the dotted blue line beyond which $SrRuO_3$ will decompose into $Sr_4Ru_3O_{10}$ and RuO_x(g). Similar breakdown under highly oxidizing conditions has been reported to occur at the surface of $SrRuO_3$ thin films.[82] On the low-temperature side, bounded by the dotted green line, excess ruthenium will precipitate as RuO_2(s).

The dashed lines, representing phase equilibria between various $Sr_{n+1}Ru_nO_{3n+1}$ RP phases with RuO_x(g), shift toward the upper left hand corner of the TOMBE diagram with increasing RuO_x(g) partial pressure. The RuO_x(g) partial pressure is determined by the excess ruthenium flux, which is another parameter that can be tuned to navigate around the thermodynamic growth window. The adsorption-controlled window for the other $Sr_{n+1}Ru_nO_{3n+1}$ RP phases, for example, Sr_2RuO_4, which is stable between the dashed red and dashed gold lines, is much narrower likely due to the very similar free energies of formation of these RP phases as is the case for $Sr_{n+1}Ti_nO_{3n+1}$ RP phases.[83]

During MBE growth, it is straightforward to provide an excess flux of ruthenium since ruthenium and strontium are evaporated from separate independent sources. Excess ruthenium flux is critical for accessing this adsorption-controlled growth window for ruthenates.

A similar TOMBE diagram [Fig. 1(b)] was calculated for the $Ca_{n+1}Ru_nO_{3n+1}$ RP series. The thermodynamic data for $Ca_{n+1}Ru_nO_{3n+1}$ are from electrochemical cell measurements,[84] while the thermodynamic data for ruthenium oxides are from the work of Rard.[17] In Fig. 1(b), the blue, gold, and red solid lines represent the equilibrium of $CaRuO_3$(s), $Ca_3Ru_2O_7$(s), and Ca_2RuO_4(s) with Ru(s), respectively. The dotted versions of the corresponding lines represent equilibria between the same phases and RuO_x(g).

The light-green shaded region in Fig. 1(b) is the adsorption-controlled growth window for $CaRuO_3$ within which solid $CaRuO_3$ is in equilibrium with RuO_x ($x = 2$ or 3) gas. The adsorption-controlled growth window for $CaRuO_3$ is much narrower than that for $SrRuO_3$. This is due to the greater difference in Gibbs formation energy between $SrRuO_3$ and RuO_2 than between $CaRuO_3$ and RuO_2. A similar growth window has been proposed for the growth of $Sr_{n+1}Ir_nO_{3n+1}$ RP phases.[85]

We use ozone as an oxidant due to its high oxidation potential, which enables us to access high oxygen activity regions of the TOMBE diagram without exceeding a chamber background pressure of 10^{-6} Torr. Total chamber pressures exceeding 10^{-6} Torr can oxidize the source materials inside effusion cells causing flux instabilities.[86–89]

The following equation describes how the ozone partial pressure at the substrate can be converted to an equivalent partial pressure of molecular oxygen,[90] p_{O_2}, where p_{O_3} is the ozone partial pressure at the substrate, ΔG^0 is the standard free energy of formation of ozone from oxygen, and T_s is the substrate temperature (where ozone decomposition occurs):

$$p_{O_2} = {p_{O_3}}^{2/3} \exp\left[\frac{\Delta G^0}{\mathrm{R}T_s}\right]. \tag{2}$$

The cyan lines in the TOMBE diagrams [Figs. 1(a) and 1(b)] are ozone oxidation potential lines for a range (10^{-11} to 10^{-5} Torr) of ozone partial pressures.

Note that we have not included RuO_4(g) in the RuO_x(g) gas phase in our thermodynamic calculations for Figs. 1(a) and 1(b). The effect of including RuO_4(g) on the TOMBE diagrams of the $Sr_{n+1}Ru_nO_{3n+1}$ and $Ca_{n+1}Ru_nO_{3n+1}$ RP phases are depicted in Figs. S5(b) and S6(b) of the supplementary material, respectively. Figure S5 of the supplementary material shows a side-by-side comparison of the $Sr_{n+1}Ru_nO_{3n+1}$ TOMBE diagram without and with the inclusion of RuO_4(g), and Fig. S6 of the supplementary material shows the comparison for the $Ca_{n+1}Ru_nO_{3n+1}$ diagrams. The effect of this inclusion on the $SrRuO_3$ growth window in the $Sr_{n+1}Ru_nO_{3n+1}$ TOMBE diagram can be seen to be minimal. If, however, we include RuO_4(g) in our calculations for the $Ca_{n+1}Ru_nO_{3n+1}$ diagram, the adsorption-controlled growth window for $CaRuO_3$ and RuO_2 does not overlap with the range of accessible ozone partial pressures [cyan lines in Figs. S6(a) and S6(b) of the supplementary material], implying that it should be impossible to grow $CaRuO_3$ and RuO_2 in an ozone ambient. This contradicts our demonstrated ability to grow these phases by MBE (as is shown, for example, in Fig. S4 of the supplementary material). Excluding RuO_4(g) in the calculations can be further justified by the fact that RuO_4(g) is likely formed by the oxidation of RuO_3(g) in the gas phase.[18,91] Therefore, it is unlikely that RuO_4(g) will be a significant component of the RuO_x(g) gas phase under the low pressure conditions encountered during MBE growth where interaction between species in the gas phase is minimal due to the long mean free paths.

Having established the thermodynamic basis for the adsorption-controlled growth of $SrRuO_3$ and $CaRuO_3$, we now turn to the growth and characterization of optimized films. We grew a 32 nm thick $SrRuO_3$ thin film on a (100) $SrTiO_3$ substrate at a temperature of 700 °C and a chamber background pressure of 10^{-6} Torr of (∼80% O_3 + 20% O_2). We used a strontium flux of 1.5×10^{13} atoms/cm^2 s and a ruthenium flux that was 2.3 times the strontium flux. We also grew a 38 nm thick $CaRuO_3$ thin film on a (110) $NdGaO_3$ substrate at a substrate temperature of 685 °C and a chamber background pressure of 10^{-6} Torr of (∼10% O_3 + 90% O_2). We used a calcium flux of 2×10^{13} atoms/cm^2 s and a ruthenium flux that was 2.6 times the calcium flux. These conditions fall within the growth window indicated in Fig. 1(a) for $SrRuO_3$. In the case of $CaRuO_3$, however, our growth conditions fall outside the calculated growth window [Fig. 1(b)] for $CaRuO_3$ on the higher temperature and higher oxygen pressure side of the TOMBE diagram. In this region of the TOMBE diagram, $CaRuO_3$ decomposes through successive oxidation to higher n members of the RP-series with the final decomposition product being CaO and RuO_x(g). We believe that $CaRuO_3$ growth is possible outside the thermodynamic window due to the relatively low growth temperature, which kinetically suppresses the oxidative decomposition of $CaRuO_3$. This is similar to the epitaxial growth of metastable alloys at low substrate temperatures to kinetically suppress thermodynamic phase separation.[92–102] The growth window outlined above works well provided there is a sufficiently high oxidant flux to avoid any oxidation kinetics issues.[69] At the end of the film growth, the strontium/calcium and ruthenium shutters were closed simultaneously and the samples were rapidly cooled under the same ozone pressure as that used during growth until the substrate temperature was below 250 °C.

Reflection high-energy electron diffraction (RHEED) was used to monitor the film growth. The RHEED pattern recorded at the end of growth (Fig. S1 of the supplementary material), while the film was still at growth temperature, consisted of spots on an arc (the Laue zone) for both the $SrRuO_3$ and the $CaRuO_3$ films indicative of two-dimensional growth. The RHEED patterns of the $CaRuO_3$ film [Figs. S1(c) and S1(d) of the supplementary material] show strong half-order peaks along both the $\langle 100\rangle_p$ and $\langle 110\rangle_p$ azimuths likely due to the strong octahedral distortions in $CaRuO_3$ that result in a doubling of the unit cell in bulk $CaRuO_3$ along these directions.[103]

X-ray diffraction (XRD) measurements were carried out in a Rigaku SmartLab high-resolution diffractometer. The indices given for $SrRuO_3$, $CaRuO_3$, and $NdGaO_3$ all correspond to the non-standard *Pbnm* setting of space group #62, where the *c*-axis is the longest axis of the unit cell. The θ-2θ XRD scans of a $SrRuO_3$ film grown on (100) $SrTiO_3$ and a $CaRuO_3$ film grown on (110) $NdGaO_3$ are shown in Figs. 2(a) and 2(b), respectively. These XRD patterns are free of spurious peaks indicating that the films are single-phase. The presence of Laue oscillations [insets to Figs. 2(a) and 2(b)] show that the films have good crystallinity and smooth interfaces. Rocking curve measurements in ω around the 220 reflections of $SrRuO_3$ [Fig. 2(c)] and $CaRuO_3$ [Fig. 2(d)], respectively, indicate that the rocking curve full width at half maximum (FWHM) of the films is comparable to the substrates upon which they are grown. Specifically the $SrRuO_3$ film had a FWHM of 40 arc sec compared to the 38 arc sec FWHM of the underlying $SrTiO_3$ substrate. Similarly, the $CaRuO_3$ film exhibited a FWHM of 13 arc sec compared to the 11 arc sec FWHM of the $NdGaO_3$ substrate upon which it was grown. These values confirm that the films have high structural perfection.

XRD ϕ scans [Fig. S2(b) of the supplementary material] confirm that the $CaRuO_3$ film grown on (110) $NdGaO_3$ is untwinned with respect to the in-plane *c*-axis orientation of the film and follows the in-plane crystallographic orientation of the isostructural substrate. This is further confirmed by imaging the RuO_6 octahedral rotations using annular bright-field scanning transmission electron microscopy (ABF-STEM).[104] XRD ϕ scans [Fig. S2(a) of the supplementary material] also reveal that the $SrRuO_3$ film on (100) $SrTiO_3$ appears to be untwinned with respect to the in-plane *c*-axis orientation even though the (100) $SrTiO_3$ substrate has 4-fold rotational symmetry. The miscut of the underlying $SrTiO_3$ substrate was measured to be 0.17° with the miscut direction perpendicular to the *c*-axis of the $SrRuO_3$ film. This agrees with the observation of other groups that the surface step edges on the $SrTiO_3$ substrate promote the nucleation of a single domain throughout the film below the tetragonal-to-orthorhombic transition of the $SrRuO_3$ film.[105–107]

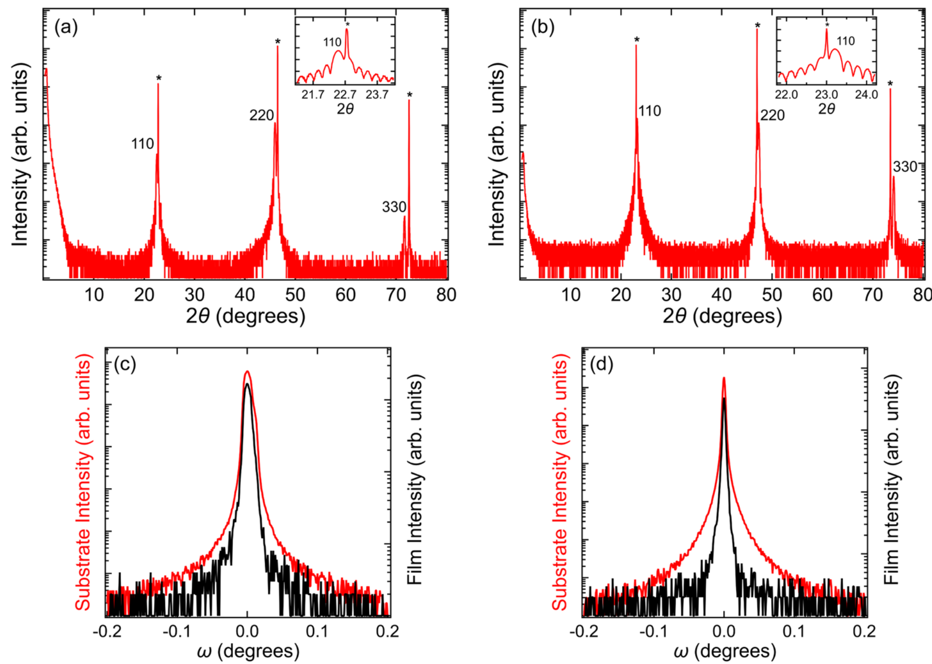

FIG. 2. X-ray diffraction scans of a 32 nm thick $SrRuO_3$ film grown on a (100) $SrTiO_3$ substrate and a 38 nm thick $CaRuO_3$ film grown on a (110) $NdGaO_3$ substrate. θ-2θ scans of (a) the $SrRuO_3$ film and (b) the $CaRuO_3$ film illustrating phase-pure growth. The insets show clear Laue oscillations indicative of a smooth film (uniform film thickness). Rocking curves in ω of (c) the $SrRuO_3$ film and (d) the $CaRuO_3$ film. The narrow peaks indicate high structural quality. In both cases, the FWHM of the film peaks are comparable to those of the underlying substrates upon which they were grown.

Cross-sectional transmission electron microscopy specimens were prepared using the standard focused ion beam (FIB) lift-out process on an FEI Strata 400 FIB equipped with an Omniprobe AutoProbe 200 nanomanipulator. Following sample preparation, the TEM specimens were imaged on an aberration-corrected 300 keV FEI Titan Themis with a probe convergence semi-angle of 30 mrad. High-angle annular dark-field scanning transmission electron microscopy (HAADF-STEM) images were acquired with inner and outer collection angles of 68 and 340 mrad, respectively, from both the 32 nm thick $SrRuO_3$ film grown on the $SrTiO_3$ substrate [Fig. 3(a)] and the 38 nm thick $CaRuO_3$ film grown on the $NdGaO_3$ substrate [Fig. 3(b)]. As electrons scattered to high angles are collected in the HAADF detector, atomic columns occupied by a higher atomic number (Z) appear brighter whereas those with a lower Z show darker contrast.

The uniform growth of the $SrRuO_3$ film on the $SrTiO_3$ substrate can be seen from the HAADF-STEM image in Fig. 3(a). Due to the higher Z of the B-site ruthenium in the film than the B-site titanium in the substrate, the film appears brighter. Furthermore, while the HAADF intensities from ruthenium (Z = 44) and strontium (Z = 38) in the $SrRuO_3$ film are rather difficult to distinguish by eye due to their similar Z, a line profile along the film's growth direction clearly displays the alternating intensities arising from the occupancy of ruthenium and strontium as shown in Fig. S7 of the supplementary material. Similarly, the uniform growth of $CaRuO_3$ on $NdGaO_3$ can be confirmed from the HAADF-STEM image in Fig. 3(b) as the contrast between the A- and B-site cations are reversed for $CaRuO_3$ and $NdGaO_3$ arising from the B-site ruthenium having a higher Z than the A-site calcium in $CaRuO_3$, while in $NdGaO_3$ the A-site neodymium has a higher Z than the B-site gallium.

The resistivity of the same $SrRuO_3$ and $CaRuO_3$ samples was measured in a van der Pauw geometry as a function of temperature. The results are shown in Fig. 4. With RRRs of 76 for $SrRuO_3$ and 75 for $CaRuO_3$, the advantage of growing ruthenate films under adsorption-controlled conditions is evident. The transport properties of ruthenates are highly sensitive to structural disorder induced by cation non-stoichiometry including point and planar defects.[19] This is usually reflected in the low RRR of films grown under non-optimized conditions. Growth under optimized conditions, outlined earlier, resulted in films with high RRRs likely due to a reduction in defects related to cation non-stoichiometry.

Note that adsorption-controlled growth conditions are not synonymous with perfect composition control. Adsorption-controlled growth conditions access the single-phase region of $SrRuO_3$ and $CaRuO_3$, but depending on how wide the composition range is of single-phase $SrRuO_3$ and $CaRuO_3$ and from which side it is approached (in our case the ruthenium-rich side)—factors that change with growth temperature and chemical potentials—the stoichiometry of the resulting film will change

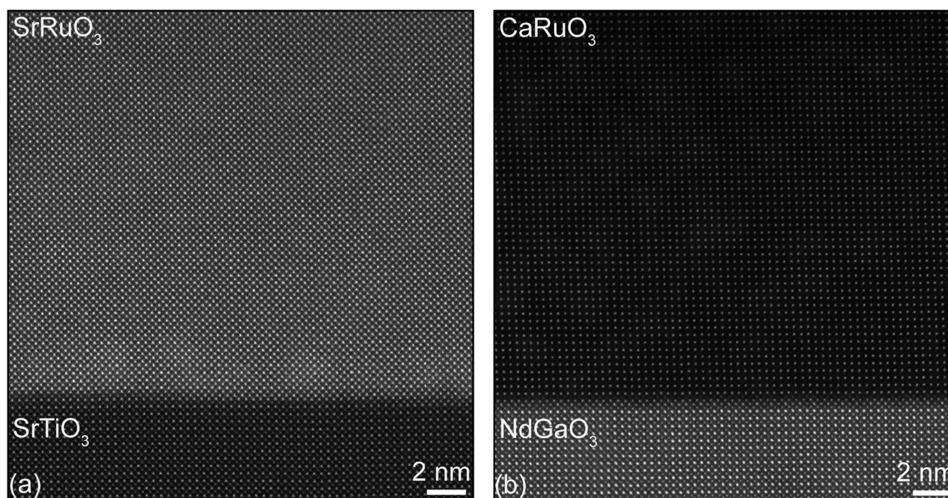

FIG. 3. HAADF-STEM images of the same (a) $SrRuO_3$ film and (b) $CaRuO_3$ film measured in Fig. 2, illustrating a sharp substrate-film interface and uniform growth.

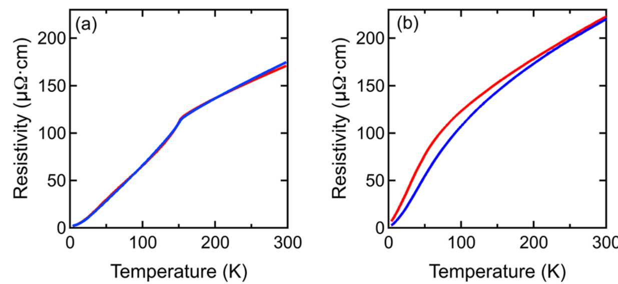

FIG. 4. Resistivity vs. temperature of the same (a) $SrRuO_3$ and (b) $CaRuO_3$ films measured in Fig. 2. The RRR ($\rho_{300\ K}/\rho_{4\ K}$) of the $CaRuO_3$ film is anisotropic. The RRR is 75 along the [001] direction (blue curve) and 31 along the [1$\bar{1}$0] direction (red curve). The RRR of the $SrRuO_3$ film is 76 and is isotropic.

though it will always remain single phase. This is analogous to the growth of III-V compound semiconductors, where this behavior is utilized to controllably alter point defect concentrations, e.g., the EL2 defect in GaAs.[108]

It is evident from Fig. 4(b) that the $CaRuO_3$ films grown on $NdGaO_3$ exhibit anisotropic electrical transport in the in-plane directions. Although the room temperature resistivities [Fig. 4(b)] are similar along the [001] and [1$\bar{1}$0] directions, the RRR along the [001] direction is significantly higher than that along the [1$\bar{1}$0] direction. This is likely due to the highly anisotropic Fermi surface of $CaRuO_3$, which has been revealed by angle-resolved photoemission spectroscopy (ARPES) measurements on our $CaRuO_3$/$NdGaO_3$(110) thin films.[109] Similar anisotropy in electrical transport has been observed for $CaRuO_3$/$NdGaO_3$(110) films grown using pulsed-laser deposition (PLD).[110] The RRR of 75 measured along [001] for our $CaRuO_3$ film is the highest of any $CaRuO_3$ films reported to date. For $SrRuO_3$, our film has a comparable RRR to that of the highest report.[73]

In summary, we have employed a combined phase stability diagram (TOMBE diagram) pertinent to MBE growth and outlined a thermodynamic growth window for the reproducible growth of $SrRuO_3$ and $CaRuO_3$ thin films with high RRR. Although the exact growth parameters might not be directly transferable from one growth chamber to another, the thermodynamic window outlined can be used as a guide while tuning synthesis conditions to grow ruthenate perovskite thin films with high RRR. The effects of moving into and out of the desired growth window can be seen directly in RHEED as shown in Figs. S3 and S4 of the supplementary material.

See supplementary material for more details on the reactions taken into account for constructing the TOMBE diagrams together with additional characterization of the films shown in Fig. 2 by RHEED, XRD, and HAADF-STEM.

H.P.N., N.J.S., and D.G.S. acknowledge support by ASCENT, one of six centers in JUMP, a Semiconductor Research Corporation (SRC) program sponsored by DARPA and from the W.M. Keck Foundation. N.J.S. acknowledges support from the National Science Foundation Graduate Research Fellowship Program under Grant No. DGE-1650441. K.M.S. and J.P.R. would like to acknowledge the National Science Foundation (No. DMR-1709255) for support. This research is funded in part by the Gordon and Betty Moore Foundation's EPiQS Initiative through Grant No. GBMF3850 to Cornell University. D.J.B. and L.F.K. acknowledge support by the Department of Defense Air Force Office of Scientific Research (No. FA 9550-16-1-0305). This work made use of the Cornell Center for Materials Research (CCMR) Shared Facilities, which are supported through the NSF MRSEC Program (No. DMR-1719875). The FEI Titan Themis 300 was acquired through No. NSF-MRI-1429155, with additional support from Cornell University, the Weill Institute, and the Kavli Institute at Cornell. Substrate preparation was performed in part at the Cornell NanoScale Facility, a member of the National Nanotechnology Coordinated Infrastructure (NNCI), which is supported by the NSF (Grant No. ECCS-15420819). S.L.S. and Z.K.L. acknowledge the support by the Pennsylvania State University ICS Seed Grant (No. 424-36 1001 cc: LIU SEED, 2017).

[1] A. P. Mackenzie and Y. Maeno, Rev. Mod. Phys. **75**, 657 (2003).
[2] S. A. Grigera, R. S. Perry, A. J. Schofield, M. Chiao, S. R. Julian, G. G. Lonzarich, S. I. Ikeda, Y. Maeno, A. J. Millis, and A. P. Mackenzie, Science **294**, 329 (2001).
[3] S. A. Grigera, P. Gegenwart, R. A. Borzi, F. Weickert, A. J. Schofield, R. S. Perry, T. Tayama, T. Sakakibara, Y. Maeno, A. G. Green, and A. P. Mackenzie, Science **306**, 1154 (2004).
[4] R. A. Borzi, S. A. Grigera, J. Farrell, R. S. Perry, S. J. S. Lister, S. L. Lee, D. A. Tennant, Y. Maeno, and A. P. Mackenzie, Science **315**, 214 (2007).
[5] A. P. Mackenzie, R. K. W. Haselwimmer, A. W. Tyler, G. G. Lonzarich, Y. Mori, S. Nishizaki, and Y. Maeno, Phys. Rev. Lett. **80**, 161 (1998).
[6] M. A. Zurbuchen, Y. Jia, S. Knapp, A. H. Carim, D. G. Schlom, L.-N. Zou, and Y. Liu, Appl. Phys. Lett. **78**, 2351 (2001).
[7] M. Schneider, D. Geiger, S. Esser, U. S. Pracht, C. Stingl, Y. Tokiwa, V. Moshnyaga, I. Sheikin, J. Mravlje, M. Scheffler, and P. Gegenwart, Phys. Rev. Lett. **112**, 206403 (2014).
[8] A. Callaghan, C. W. Moeller, and R. Ward, Inorg. Chem. **5**, 1572 (1966).
[9] Y. Maeno, H. Hashimoto, K. Yoshida, S. Nishizaki, T. Fujita, J. G. Bednorz, and F. Lichtenberg, Nature **372**, 532 (1994).
[10] G. Cao, C. S. Alexander, S. McCall, J. E. Crow, and R. P. Guertin, Mater. Sci. Eng. B **63**, 76 (1999).
[11] C. W. Hicks, D. O. Brodsky, E. A. Yelland, A. S. Gibbs, J. A. N. Bruin, M. E. Barber, S. D. Edkins, K. Nishimura, S. Yonezawa, Y. Maeno, and A. P. Mackenzie, Science **344**, 283 (2014).
[12] A. Steppke, L. Zhao, M. E. Barber, T. Scaffidi, F. Jerzembeck, H. Rosner, A. S. Gibbs, Y. Maeno, S. H. Simon, A. P. Mackenzie, and C. W. Hicks, Science **355**, eaaf9398 (2017).
[13] L. Miao, W. Zhang, P. Silwal, X. Zhou, I. Stern, T. Liu, J. Peng, J. Hu, D. H. Kim, and Z. Q. Mao, Phys. Rev. B **88**, 115102 (2013).
[14] S.-I. Ikeda, Y. Maeno, S. Nakatsuji, M. Kosaka, and Y. Uwatoko, Phys. Rev. B **62**, R6089 (2000).
[15] F. Nakamura, T. Goko, M. Ito, T. Fujita, S. Nakatsuji, H. Fukazawa, Y. Maeno, P. Alireza, D. Forsythe, and S. R. Julian, Phys. Rev. B **65**, 220402 (2002).
[16] W. E. Bell and M. Tagami, J. Phys. Chem. **67**, 2432 (1963).
[17] J. A. Rard, Chem. Rev. **85**, 1 (1985).
[18] F. Garisto, *Thermodynamic Behaviour of Ruthenium at High Temperatures* (Atomic Energy of Canada Ltd., Pinawa, MB, Canada, 1988).
[19] W. Siemons, G. Koster, A. Vailionis, H. Yamamoto, D. H. A. Blank, and M. R. Beasley, Phys. Rev. B **76**, 075126 (2007).
[20] N. Okuda, K. Saito, and H. Funakubo, Jpn. J. Appl. Phys., Part 1 **39**, 572 (2000).
[21] G. Rijnders, D. H. A. Blank, J. Choi, and C.-B. Eom, Appl. Phys. Lett. **84**, 505 (2004).
[22] G. Koster, L. Klein, W. Siemons, G. Rijnders, J. S. Dodge, C.-B. Eom, D. H. A. Blank, and M. R. Beasley, Rev. Mod. Phys. **84**, 253 (2012).
[23] P. Khalifah, I. Ohkubo, H. M. Christen, and D. G. Mandrus, Phys. Rev. B **70**, 134426 (2004).
[24] L. Klein, L. Antognazza, T. H. Geballe, M. R. Beasley, and A. Kapitulnik, Phys. Rev. B **60**, 1448 (1999).
[25] S. Tripathi, R. Rana, S. Kumar, P. Pandey, R. S. Singh, and D. S. Rana, Sci. Rep. **4**, 3877 (2014).
[26] M. Wissinger, D. Fuchs, L. Dieterle, H. Leiste, R. Schneider, D. Gerthsen, and H. V. Löhneysen, Phys. Rev. B **83**, 144430 (2011).
[27] H. F. Yang, C. C. Fan, Z. T. Liu, Q. Yao, M. Y. Li, J. S. Liu, M. H. Jiang, and D. W. Shen, Phys. Rev. B **94**, 115151 (2016).
[28] B. Dabrowski, O. Chmaissem, P. W. Klamut, S. Kolesnik, M. Maxwell, J. Mais, Y. Ito, B. D. Armstrong, J. D. Jorgensen, and S. Short, Phys. Rev. B **70**, 014423 (2004).
[29] Q. X. Jia, F. Chu, C. D. Adams, X. D. Wu, M. Hawley, J. H. Cho, A. T. Findikoglu, S. R. Foltyn, J. L. Smith, and T. E. Mitchell, J. Mater. Res. **11**, 2263 (1996).
[30] G. Siegel, G. Pfennigsdorf, and H. Mönig, Naturwissenschaften **45**, 415 (1958).
[31] J. R. Arthur, J. Appl. Phys. **39**, 4032 (1968).
[32] A. Y. Cho, Surf. Sci. **17**, 494 (1969).
[33] A. Y. Cho, J. Appl. Phys. **41**, 2780 (1970).
[34] A. Y. Cho, J. Appl. Phys. **42**, 2074 (1971).
[35] H. Freller and K. G. Günther, Thin Solid Films **88**, 291 (1982).
[36] R. Heckingbottom, G. J. Davies, and K. A. Prior, Surf. Sci. **132**, 375 (1983).
[37] H. Seki and A. Koukitu, J. Cryst. Growth **78**, 342 (1986).
[38] J. Y. Tsao, J. Cryst. Growth **110**, 595 (1991).
[39] G. J. M. Dormans, P. J. Van Veldhoven, and M. De Keijser, J. Cryst. Growth **123**, 537 (1992).
[40] C. D. Theis and D. G. Schlom, J. Cryst. Growth **174**, 473 (1997).
[41] S. Migita, Y. Kasai, H. Ota, and S. Sakai, Appl. Phys. Lett. **71**, 3712 (1997).
[42] C. D. Theis, J. Yeh, D. G. Schlom, M. E. Hawley, G. W. Brown, J. C. Jiang, and X. Q. Pan, Appl. Phys. Lett. **72**, 2817 (1998).
[43] C. D. Theis, J. Yeh, D. G. Schlom, M. E. Hawley, and G. W. Brown, Thin Solid Films **325**, 107 (1998).
[44] S. Migita, H. Ota, H. Fujino, Y. Kasai, and S. Sakai, J. Cryst. Growth **200**, 161 (1999).
[45] D. G. Schlom, J. H. Haeni, J. Lettieri, C. D. Theis, W. Tian, J. C. Jiang, and X. Q. Pan, Mater. Sci. Eng.: B **87**, 282 (2001).
[46] H. Ott, S. J. Heise, R. Sutarto, Z. Hu, C. F. Chang, H. H. Hsieh, H.-J. Lin, C. T. Chen, and L. H. Tjeng, Phys. Rev. B **73**, 094407 (2006).
[47] J. F. Ihlefeld, A. Kumar, V. Gopalan, D. G. Schlom, Y. B. Chen, X. Q. Pan, T. Heeg, J. Schubert, X. Ke, P. Schiffer, J. Orenstein, L. W. Martin, Y. H. Chu, and R. Ramesh, Appl. Phys. Lett. **91**, 071922 (2007).
[48] J. Kabelac, S. Ghosh, P. Dobal, and R. Katiyar, J. Vac. Sci. Technol., B: Microelectron. Nanometer Struct.–Process., Meas., Phenom. **25**, 1049 (2007).
[49] G. Rispens and B. Noheda, Integr. Ferroelectr. **92**, 30 (2007).

[50] J. F. Ihlefeld, N. J. Podraza, Z. K. Liu, R. C. Rai, X. Xu, T. Heeg, Y. B. Chen, J. Li, R. W. Collins, J. L. Musfeldt, X. Q. Pan, J. Schubert, R. Ramesh, and D. G. Schlom, Appl. Phys. Lett. **92**, 142908 (2008).
[51] R. W. Ulbricht, A. Schmehl, T. Heeg, J. Schubert, and D. G. Schlom, Appl. Phys. Lett. **93**, 102105 (2008).
[52] R. Sutarto, S. G. Altendorf, B. Coloru, M. Moretti Sala, T. Haupricht, C. F. Chang, Z. Hu, C. Schüßler-Langeheine, N. Hollmann, H. Kierspel, H. H. Hsieh, H.-J. Lin, C. T. Chen, and L. H. Tjeng, Phys. Rev. B **79**, 205318 (2009).
[53] J. F. Ihlefeld, Z.-K. L. Wei Tian, W. A. Doolittle, M. Bernhagen, P. Reiche, R. Uecker, R. Ramesh, and D. G. Schlom, IEEE Trans. Ultrason., Ferroelectr. Freq. Control **56**, 1528 (2009).
[54] B. Jalan, R. Engel-Herbert, N. J. Wright, and S. Stemmer, J. Vac. Sci. Technol., A **27**, 461 (2009).
[55] M. D. Losego, H. S. Craft, E. A. Paisley, S. Mita, R. Collazo, Z. Sitar, and J. P. Maria, J. Mater. Res. **25**, 670 (2010).
[56] J. H. Lee, X. Ke, R. Misra, J. F. Ihlefeld, X. S. Xu, Z. G. Mei, T. Heeg, M. Roeckerath, J. Schubert, Z. K. Liu, J. L. Musfeldt, P. Schiffer, and D. G. Schlom, Appl. Phys. Lett. **96**, 262905 (2010).
[57] C. M. Brooks, R. Misra, J. A. Mundy, L. A. Zhang, B. S. Holinsworth, K. R. O'Neal, T. Heeg, W. Zander, J. Schubert, J. L. Musfeldt, Z.-K. Liu, D. A. Muller, P. Schiffer, and D. G. Schlom, Appl. Phys. Lett. **101**, 132907 (2012).
[58] P. Moetakef, J. Y. Zhang, S. Raghavan, A. P. Kajdos, and S. Stemmer, J. Vac. Sci. Technol., A **31**, 041503 (2013).
[59] S. Stoughton, M. Showak, Q. Mao, P. Koirala, D. A. Hillsberry, S. Sallis, L. F. Kourkoutis, K. Nguyen, L. F. J. Piper, D. A. Tenne, N. J. Podraza, D. A. Muller, C. Adamo, and D. G. Schlom, APL Mater. **1**, 042112 (2013).
[60] J. A. Moyer, C. Eaton, and R. Engel-Herbert, Adv. Mater. **25**, 3578 (2013).
[61] M. Uchida, Y. F. Nie, P. D. C. King, C. H. Kim, C. J. Fennie, D. G. Schlom, and K. M. Shen, Phys. Rev. B **90**, 075142 (2014).
[62] Y. Matsubara, K. S. Takahashi, Y. Tokura, and M. Kawasaki, Appl. Phys. Express **7**, 125502 (2014).
[63] Y. F. Nie, P. D. C. King, C. H. Kim, M. Uchida, H. I. Wei, B. D. Faeth, J. P. Ruf, J. P. C. Ruff, L. Xie, X. Pan, C. J. Fennie, D. G. Schlom, and K. M. Shen, Phys. Rev. Lett. **114**, 016401 (2015).
[64] H.-T. Zhang, L. R. Dedon, L. W. Martin, and R. Engel-Herbert, Appl. Phys. Lett. **106**, 233102 (2015).
[65] M. Brahlek, L. Zhang, C. Eaton, H.-T. Zhang, and R. Engel-Herbert, Appl. Phys. Lett. **107**, 143108 (2015).
[66] J. K. Kawasaki, M. Uchida, H. Paik, D. G. Schlom, and K. M. Shen, Phys. Rev. B **94**, 121104 (2016).
[67] B. Burganov, C. Adamo, A. Mulder, M. Uchida, P. D. C. King, J. W. Harter, D. E. Shai, A. S. Gibbs, A. P. Mackenzie, R. Uecker, M. Bruetzam, M. R. Beasley, C. J. Fennie, D. G. Schlom, and K. M. Shen, Phys. Rev. Lett. **116**, 197003 (2016).
[68] R. C. Haislmaier, E. D. Grimley, M. D. Biegalski, J. M. LeBeau, S. Trolier-McKinstry, V. Gopalan, and R. Engel-Herbert, Adv. Funct. Mater. **26**, 7271 (2016).
[69] E. H. Smith, J. F. Ihlefeld, C. A. Heikes, H. Paik, Y. Nie, C. Adamo, T. Heeg, Z.-K. Liu, and D. G. Schlom, Phys. Rev. Mater. **1**, 023403 (2017).
[70] A. Prakash, P. Xu, X. Wu, G. Haugstad, X. Wang, and B. Jalan, J. Mater. Chem. C **5**, 5730 (2017).
[71] P. B. Marshall, H. Kim, K. Ahadi, and S. Stemmer, APL Mater. **5**, 096101 (2017).
[72] H. Paik, Z. Chen, E. Lochocki, A. H. Seidner, A. Verma, N. Tanen, J. Park, M. Uchida, S. Shang, and B.-C. Zhou, APL Mater. **5**, 116107 (2017).
[73] M. Izumi, K. Nakazawa, Y. Bando, Y. Yoneda, and H. Terauchi, J. Phys. Soc. Jpn. **66**, 3893 (1997).
[74] N. Kikugawa, R. Baumbach, J. S. Brooks, T. Terashima, S. Uji, and Y. Maeno, Cryst. Growth Des. **15**, 5573 (2015).
[75] L. Capogna, A. P. Mackenzie, R. S. Perry, S. A. Grigera, L. M. Galvin, P. Raychaudhuri, A. J. Schofield, C. S. Alexander, G. Cao, S. R. Julian, and Y. Maeno, Phys. Rev. Lett. **88**, 076602 (2002).
[76] V. Leca, D. H. A. Blank, and G. Rijnders, e-print arXiv:1202.2256 (2012).
[77] G. Koster, G. Rijnders, D. H. A. Blank, and H. Rogalla, Phys. C **339**, 215 (2000).
[78] D. Balz and K. Plieth, Z. Elektrochem., Bet. Bunsenges. Physik. Chem. **59**, 545 (1955).
[79] S. N. Ruddlesden and P. Popper, Acta Crystallogr. **10**, 538 (1957).
[80] S. N. Ruddlesden and P. Popper, Acta Crystallogr. **11**, 54 (1958).
[81] K. T. Jacob, K. T. Lwin, and Y. Waseda, Mater. Sci. Eng.: B **103**, 152 (2003).
[82] J. Shin, S. V. Kalinin, H. N. Lee, H. M. Christen, R. G. Moore, E. W. Plummer, and A. P. Baddorf, Surf. Sci. **581**, 118 (2005).
[83] K. R. Udayakumar and A. N. Cormack, J. Am. Ceram. Soc. **71**, C469 (1988).
[84] K. T. Jacob, K. T. Lwin, and Y. Waseda, J. Electrochem. Soc. **150**, E227 (2003).
[85] K. Nishio, H. Y. Hwang, and Y. Hikita, APL Mater. **4**, 036102 (2016).
[86] E. S. Hellman and E. H. Hartford, Jr., J. Vac. Sci. Technol., B: Microelectron. Nanometer Struct.–Process., Meas., Phenom. **12**, 1178 (1994).
[87] Y. S. Kim, N. Bansal, C. Chaparro, H. Gross, and S. Oh, J. Vac. Sci. Technol., A **28**, 271 (2010).
[88] Y. S. Kim, N. Bansal, and S. Oh, J. Vac. Sci. Technol., A **28**, 600 (2010).
[89] Y. S. Kim, N. Bansal, and S. Oh, J. Vac. Sci. Technol., A **29**, 041505 (2011).
[90] Y. Krockenberger, J. Kurian, A. Winkler, A. Tsukada, M. Naito, and L. Alff, Phys. Rev. B **77**, 060505 (2008).
[91] M. J. Holdoway, *Volatilisation and Deposition of Ruthenium Dioxide in Relation to the Fingal Process* (Atomic Energy Research Establishment, Harwell, UK, 1971).
[92] T. Waho, S. Ogawa, and S. Maruyama, Jpn. J. Appl. Phys., Part 1 **16**, 1875 (1977).
[93] H. Munekata, H. Ohno, S. Von Molnar, A. Segmüller, L. L. Chang, and L. Esaki, Phys. Rev. Lett. **63**, 1849 (1989).
[94] M. H. Yang and C. P. Flynn, Phys. Rev. Lett. **62**, 2476 (1989).
[95] H. Holzschuh and H. Suhr, Appl. Phys. Lett. **59**, 470 (1991).
[96] E. S. Hellman and E. H. Hartford, Appl. Phys. Lett. **64**, 1341 (1994).
[97] A. Fischer, Z. Feng, E. Bykov, G. Contreras-Puente, A. Compaan, F. de Landa Castillo-Alvarado, J. Avendaño, and A. Mason, Appl. Phys. Lett. **70**, 3239 (1997).
[98] W. G. Bi and C. W. Tu, Appl. Phys. Lett. **70**, 1608 (1997).
[99] W. I. Park, G.-C. Yi, and H. M. Jang, Appl. Phys. Lett. **79**, 2022 (2001).
[100] J. Lettieri, J. H. Haeni, and D. G. Schlom, J. Vac. Sci. Technol. A **20**, 1332 (2002).

[101] M. Yoshimoto, S. Murata, A. Chayahara, Y. Horino, J. Saraie, and K. Oe, Jpn. J. Appl. Phys., Part 2 **42**, L1235 (2003).
[102] E. Iliopoulos, A. Georgakilas, E. Dimakis, A. Adikimenakis, K. Tsagaraki, M. Androulidaki, and N. T. Pelekanos, Phys. Status Solidi A **203**, 102 (2006).
[103] W. Bensch, H. W. Schmalle, and A. Reller, Solid State Ionics **43**, 171 (1990).
[104] D. Baek, H. P. Nair, J. P. Ruf, N. J. Schreiber, K. M. Shen, D. G. Schlom, and L. F. Kourkoutis (unpublished).
[105] Q. Gan, R. A. Rao, and C. B. Eom, Appl. Phys. Lett. **70**, 1962 (1997).
[106] J.-P. Maria, H. L. McKinstry, and S. Trolier-McKinstry, Appl. Phys. Lett. **76**, 3382 (2000).
[107] A. Vailionis, W. Siemons, and G. Koster, Appl. Phys. Lett. **91**, 071907 (2007).
[108] D. T. J. Hurle, J. Appl. Phys. **107**, 121301 (2010).
[109] Y. Liu, H. P. Nair, J. P. Ruf, D. G. Schlom, and K. M. Shen, "Revealing the hidden heavy Fermi liquid in $CaRuO_3$" (unpublished).
[110] D. L. Proffit, H. W. Jang, S. Lee, C. T. Nelson, X. Q. Pan, M. S. Rzchowski, and C. B. Eom, Appl. Phys. Lett. **93**, 111912 (2008).

Figure S2: XRD ! scans of the same (a) $SrRuO_3$ and (b) $CaRuO_3$ films measured in Fig. 2. Both the $SrRuO_3$ and $CaRuO_3$ films are untwinned with respect to the in-plane orientation of the !-axis of the film. For (a) and (b) the !"= 0 direction is parallel to the $[1\bar{1}0]$ axis of the film.

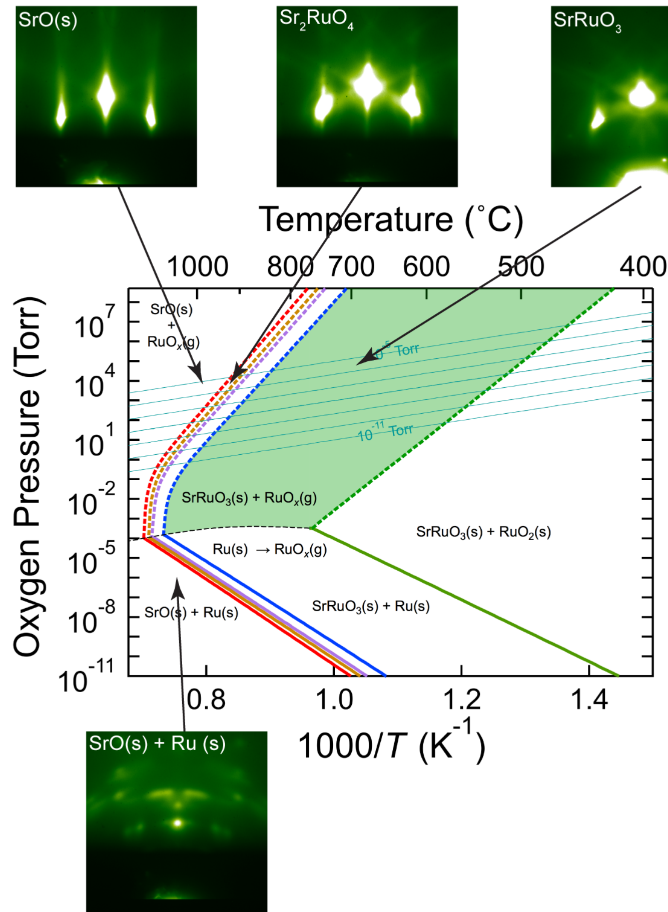

Figure S3: TOMBE diagram for $Sr_{n+1}Ru_nO_{3n+1}$ phases (the same as Fig. 1(a)) overlaid with the RHEED images taken along the <100>$_p$ azimuth during growth under various growth conditions. RHEED in combination with this TOMBE diagram enables the growth space to be navigated to achieve desired $Sr_{n+1}Ru_nO_{3n+1}$ phases.

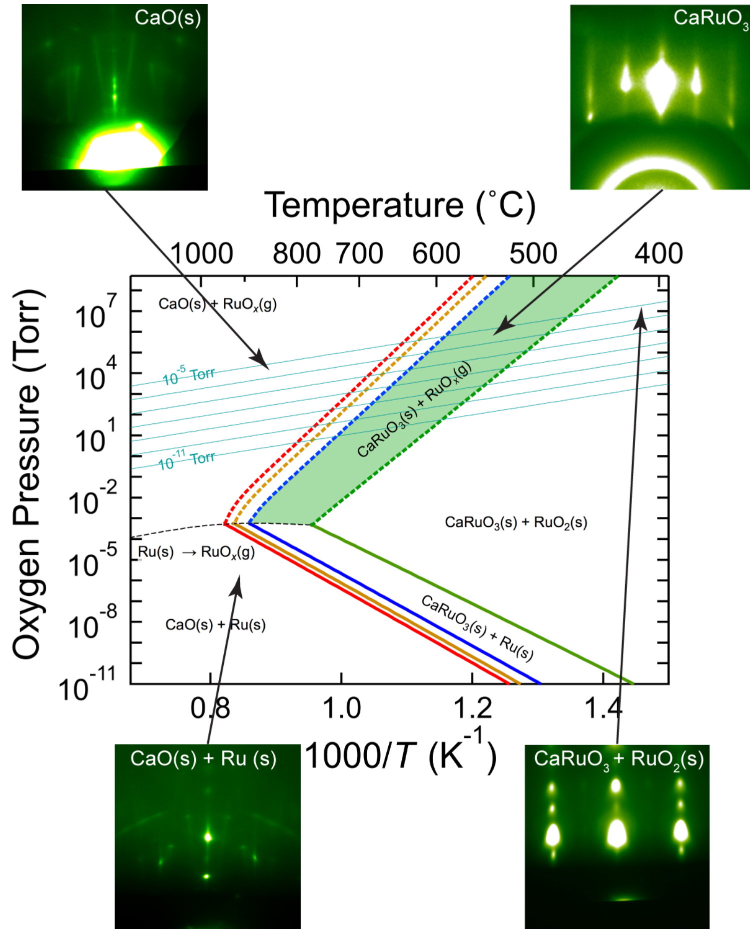

Figure S4: TOMBE diagram for $Ca_{n+1}Ru_nO_{3n+1}$ phases (the same as Fig. 1(b)) overlaid with the RHEED images taken along the <100>$_p$ azimuth during growth under various growth conditions. RHEED in combination with this TOMBE diagram enables the growth space to be navigated to achieve desired $Ca_{n+1}Ru_nO_{3n+1}$ phases. Note that the conditions under which we grow Ca_2RuO_4 films fall in the region for CaO(s) + RuO_x(g) in the TOMBE diagram. We believe that we are able to achieve Ca_2RuO_4 epitaxy due to kinetic suppression of decomposition of Ca_2RuO_4 into CaO(s) and RuO_x(g).

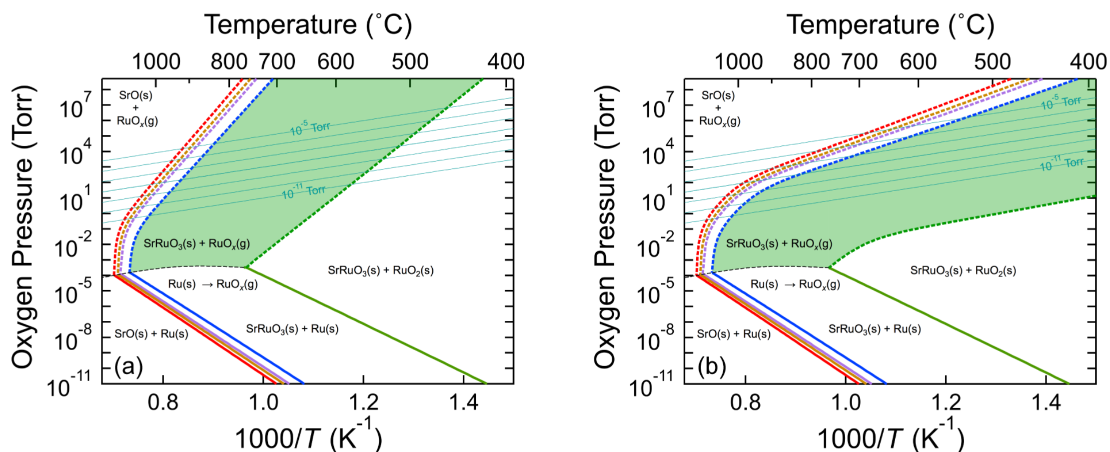

Figure S5: TOMBE diagram outlining the adsorption-controlled growth window for $Sr_{n+1}Ru_nO_{3n+1}$ phases illustrating the effect of (a) excluding RuO_4(g) and (b) including RuO_4(g) in the thermodynamic calculations.

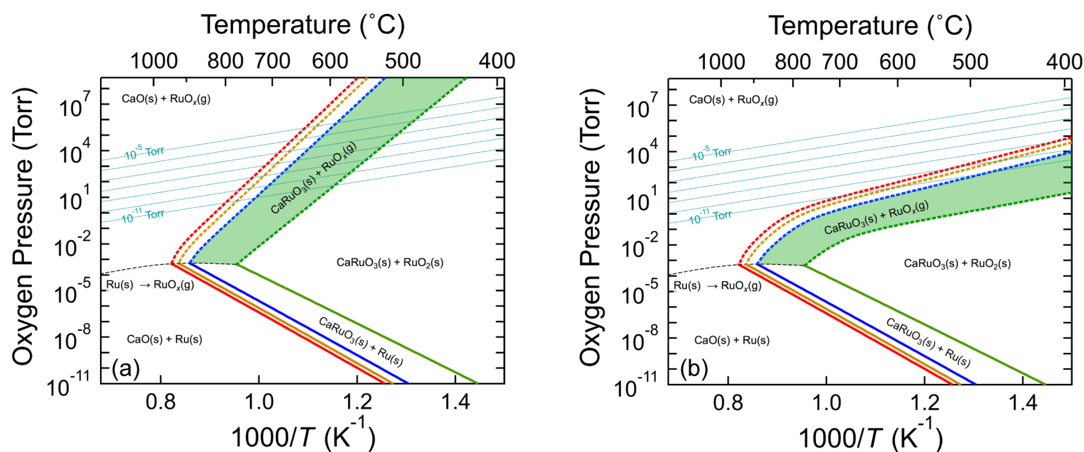

Figure S6: TOMBE diagram outlining the adsorption-controlled growth window for $Ca_{n+1}Ru_nO_{3n+1}$ phases illustrating the effect of (a) excluding RuO_4(g) and (b) including RuO_4(g) in the thermodynamic calculations.

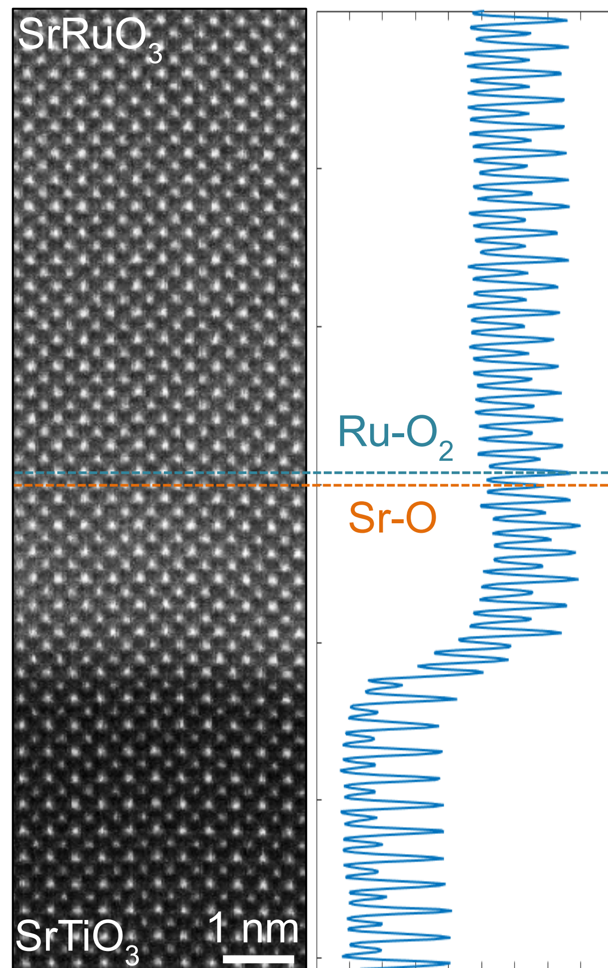

Figure S7: Intensity line profile extracted from a blown-up region of the $SrTiO_3$ substrate-$SrRuO_3$ film interface from the STEM image in Fig. 3(a) along the growth direction of the film, illustrating the alternating contrast arising from the occupancy of ruthenium and strontium in the overlying film.